IEEE Access
Multidisciplinary | Rapid Review | Open Access Journal

Received January 9, 2020, accepted March 6, 2020, date of publication March 11, 2020, date of current version March 24, 2020.

Digital Object Identifier 10.1109/ACCESS.2020.2979993

A Robot-Assisted Spine Surgery System Based on Intraoperative 2D Fluoroscopy Navigation

SHAODONG LI, ZHIJIANG DU, AND HONGJIAN YU
State Key Laboratory of Robotics and Systems, Harbin Institute of Technology, Harbin 150080, China
Corresponding author: Hongjian Yu (yuhongjian99@126.com)

This work was supported by the Chinese National High Technology Research and Development Program (863) under Grant 2015AA043201.

ABSTRACT In this paper, a robotic system based on intraoperative 2D fluoroscopy navigation in which fluoroscopy images are obtained by C-arm popularized in the clinic, for spine surgery is proposed. The procedure of robot-assisted spine surgery is designed and described. An improved special 6-dof hybrid robot considering both the stiffness and workspace is proposed. And the kinematic model and jacobian matrix of robot are established. To realize fluroscopy images acquisition and avoid interfering with the patient during the process of positioning, human-robot cooperation based on fuzzy variable admittance control considering arm stiffness which would influence the stability of robot, is applied in robotic system. In addition, navigation techniques containing a novel bi-planar design, a robust circular control point detector and closed-loop positioning of tool, based on fluoroscopy images are proposed. In experiments, kinematic model of hybrid robot is test based on laser tracker and the distance error is 0.17 mm which is much smaller than the motion range. The effect of tool weight compensation is measured and the max mean force and torque errors are 0.7477N and 0.0617 N.M. The experimental results could meet requirements in human-robot cooperation. Furthermore, we test the the robotic system proposed in this paper on spine model bone and cadaver with the help of surgeons. The experimental results are validated by 2D image c-arm-based and 3D image CT-based and considered clinically acceptable.

INDEX TERMS Robot-assisted spine surgery system, 6-dof hybrid robot, intraoperative 2D fluoroscopy navigation, spine model bone and cadaver experiments.

I. INTRODUCTION

Conventional open spine surgery is the major mean for the treatment of spinal disorders. However, the clinical outcomes, the morbidity, and the soft tissue injury are not optimal [1], [2]. Minimally invasive spine surgery (MISS) which is superior to the traditional surgery in the problems mentioned above, has obtained fast development in the past decade [3]. MISS concentrates on realizing the best outcome for patient with the smallest iatrogenic risk exposure, but this way comes at the longer learning curve which refers to the time taken by a surgeon to become proficient [4], [5], because of the increase in technical difficulty due to the unfamiliar procedures, and the decrease in visualization due to the narrow restricted surgical field [6].

The associate editor coordinating the review of this manuscript and approving it for publication was Sunil Karamchandani.

Computer-assisted orthopedic surgery (CAOS) including preoperative CT-based, intraoperative 2D fluoroscopy-based and intraoperative 3D fluoroscopy-based, could reduce the learning curve and improve accuracy and reliability for spine surgery. Preoperative CT-based navigation [7] needs the excessive preoperative preparation consisting of data acquisition and image-patient registration. Intraoperative 2D [8] and 3D [9] fluoroscopy-based navigations could tackle such problems. 2D Fluoroscopy-based navigation could reduce radiation exposure because of less imaging time and improve operating room environment by avoiding the need for real-time fluoroscopy [51]. In addition, 2D navigation is comparable to CT-based navigation assistance in the lumbar level [10] and realizes the reliable and accurate effect in low thoracic and lumbar spine surgery [49], [50]. Compared with 2D navigation, 3D navigation is more accurate [11], [52] and could solve all thoracic levels and lumbar levels [53]. However, the potential drawbacks contain expensive

TABLE 1. Comparison of different navigations.

Different navigations	Complexity [7],[8],[9],[51]	precision[10],[11],[49],[50],[52],[53]	cost[12],[13]
CT-based	High	Low	Low
2D fluoroscopy-based	Low	Low	Low
3D fluoroscopy-based	Low	High	High

equipment, higher radiation does and longer total procedure [12], [13], [54]. The comparison results of three navigations are listed in table 1. it is noticed that 2D fluoroscopy-based navigation could meet the precision for spine surgery with the low cost and operation complexity. Therefore, 2D fluoroscopy-based navigation would be adopted in this paper according to the analysis above.

Although CAOS indeed show higher accuracy and reliability in spine surgery than traditional methods, there are two main drawbacks [14]. One is that surgeons need to pay more attention to the monitor rather than patient during navigation and this would change the surgery custom of surgeons. The other is that the marker mounted on the tool need to be seen by a 3D optical localizer in real time and this would affect the operation of surgeon. Robot-assisted spine surgery could overcome the problems above and realize the comparable effects with CAOS [15]–[24]. SpineAssist [15] and Renaissance [16] have the similar spine surgery procedure in which two kinds of navigation containing preoperative CT-based and intraoperative 3D fluoroscopy-based could be selected. In 2018, the next generation Mazor X suggested for intraoperative 3D fluoroscopy-based navigation was reported [17], [18]. ROSA robot [19], [20], [21] in which the intraoperative O-arm-based navigation is applied, is also a commercial product and has higher precision compared to conventional method. TiRobot robot system [22]–[24] is the first multi-indication orthopaedic system worldwide and relies on the intraoperative 3D fluoroscopy-based navigation. It is noticed that Mazor series, ROSA, and TiRobot have entered the clinical stage. However, the expensive equipment applied in intraoperative 3D navigation system limits the clinical promotion.

In addition to the above mature robotic systems, the first generation SPINEBOT [25] based on fiducial marks registration and the second generation SPINEBOT [26] based on DRR registration were proposed by Byung-Ju Yi *et al.* The CoRA [27] derived from upgrade SPINEBOT was also presented later. A Hands-on-Robot [28] was proposed for pedicle screws insertion with fully torque controlled robot. A robot spine surgery system with a teleoperation system [29] and a body-mounted robot system [30] were presented respectively. However, most of the systems mentioned above are in experimental stage, and a few are only in theoretical stage. Furthermore, A robot navigation system [55] based on fluoroscopy images for distal locking of intramedullary nails was presented. The positioning precision of the robot was validated and the average error was 0.24 mm. However, this robotic system could not meet spine surgery.

Based on the analysis above, we propose a robotic system with intraoperative 2D fluoroscopy navigation for spine surgery. This robotic system not only meets the demands of lumbar level, but also has low requirements for intraoperative imaging equipment. The robotic system constitution and the procedure for robot-assisted spine surgery are described in section II. The hybrid robot involving robot design and kinematic model is given in section II.A. The human-robot cooperation based on variable admittance control is proposed in section II.B. And 2D navigation based on a novel bi-planar and a robust control point detector is presented in section II.C. Finally, Experiments about robot-assisted spine surgery and related technologies are implemented in section III.

II. HYBRID ROBOT SYSTEM

A robot-assisted spine surgery system is presented in this paper and shown in figure 1. The patient lies prone on the surgical bed, the passive markers are attached to the patient and robot respectively, the 3D optical positioner is used to position the tool relative to the patient, C-arm is used to obtain lateral and anterior-posterior (ap) fluoroscopy images. The procedure for spine surgery using robotic system is described in figure 2.

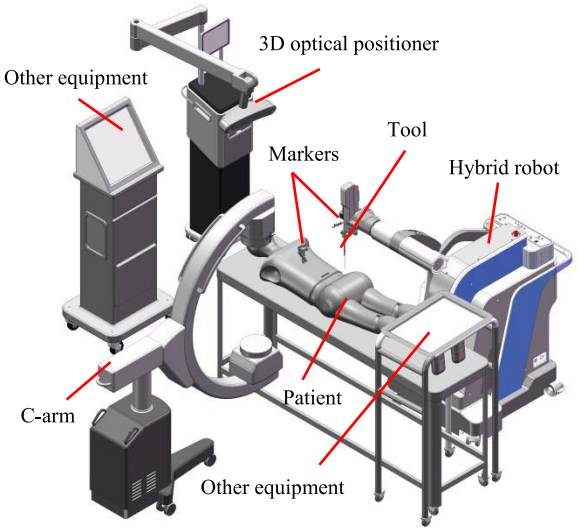

FIGURE 1. Robot-assisted spine surgery system.

1) PREOPERATIVE PREPARATION

First, the surgeons treat the patient as conventional preoperative procedures. Next, the passive marker is anchored on vertebral spinous near the interest spine level by a clamp.

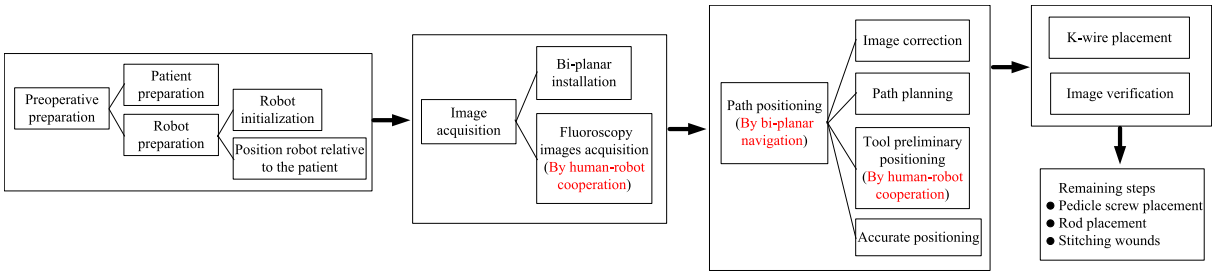

FIGURE 2. Procedure of robot-assisted spine surgery.

The clamp is used to connect the passive marker to vertebral spinous. Then, the robot is covered with the sterile bag and robotic system need to be initialized. Finally, the assistant would position the base coordinate of robot relative to the operation area of patient by pushing the robot.

2) IMAGE ACQUISITION

The bi-planar is installed to the end of the robot and is matched with the intensifier of C-arm by human-robot cooperation to obtain lateral and ap fluoroscopy images. It is noticed that all the control points need to be displayed on the images. Control points consisting of circular objects are mapped from a series of 4 mm diameter steel balls attached to the bi-planar by X-ray and the details about control points are described in [40].

3) TARGET PATH POSITIONING

First, the images derived from image acquisition are imported into software. Next, distortion correction of fluoroscopy image is implemented and target path is planned on the images by surgeons. Then, the path in image coordinate is transferred into robot coordinate. Finally, tool would arrive the target area without interference with the patient based on human-robot cooperation. And the closed-loop kinematic control could realize the accurate positioning. In fact, the navigation consists the processes mentioned above.

4) KIRSCHNER WIRE (K-WIRE) PLACEMENT AND IMAGE VERIFICATION

The k-wire would be inserted into pedicle by robotic system. Then, the safety and effectiveness of k-wire position could be verified by fluoroscopy image.

5) REMAINING STEPS

The remaining steps including pedicle screw placement, rod placement and stitching wounds, would be implemented when the k-wire position is acceptable after image verification.

According to the procedure of robot-assisted spine surgery, we could conclude that robot, human-robot cooperation and navigation are the core technologies in robotic system and proposed in this paper.

A. HYBRID ROBOT

1) HYBRID ROBOT DESIGN

There are two types in commercial robots for spine surgery. One is the parallel robot [15] which is mounted on a bridge and has high precision, stiffness but small workspace. The position of robot needs to be moved when multiple levels are encountered in surgery. Parallel robot [15] makes the surgery more complicated. The other is serial robot [20], [23] which has the advantages of large workspace and simple structure and the disadvantages of low stiffness. In [15], [20], [23], the system is only used to realize accurate positioning and the low stiffness could meet demand. However, the k-wire would be inserted into pedicle by robotic system in this paper and the stiffness of serial robot could not meet requirement. During the process of tool positioning, rotation dof around the k-wire does not need to be considered. Therefore, robot should have at least 5-dof including location of three-dimensional and orientation of two-dimensional. Furthermore, k-wire placement after tool positioning is realized by robot. Therefore, translation dof along the k-wire need to be considered in robot design.

Considering the content described above, we proposed a 6-dof hybrid robot in which the first five dofs is used to realize tool positioning and the last dof is used to place k-wires [31]. The first two joints adopt parallel mechanisms to ensure the precision and stiffness and the last four joints adopt serial mechanisms to meet the surgery workspace requirements. According to the experiments of spine model bone, we conclude that the hybrid robot proposed in [31] still has problems in joint drive and workspace. In hybrid robot, the rotational motion of joint 3 and the translational motion of joint 4 are coupled by the THK ball screw/spline and this coupled motion would pose the difficulties for kinematic control. Therefore, we improve hybrid robot in joint 3 drive and joint 4 drive. In addition, we improve structure parameters of hybrid robot to meet the demands of surgical workspace. The two-generation hybrid robots are shown in figure 3.

The improved hybrid robot consists of PRRRP planar parallel mechanism applied in the first two joints and PRRP serial mechanism applied in the last four joints. The first three joints and last joint adopt screw module driven by maxon motor to realize translational motion. The joints 4 and 5 adopt gear drive and harmonic gear reducer to realize

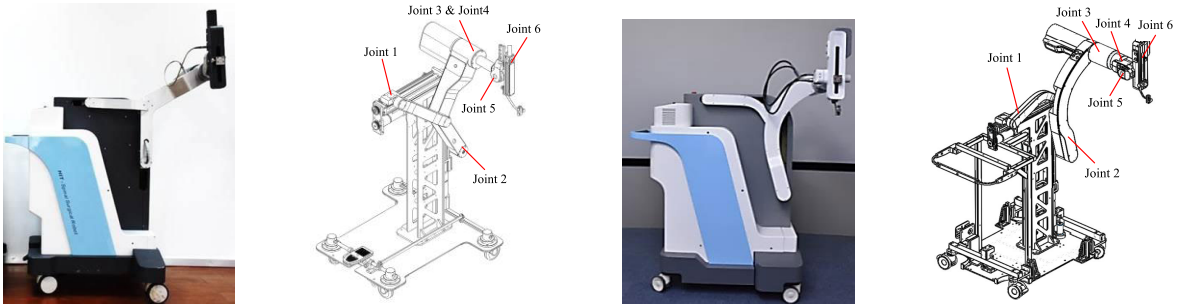

(a) Hybrid robot (b) Improved hybrid robot

FIGURE 3. Two-generation hybrid robots.

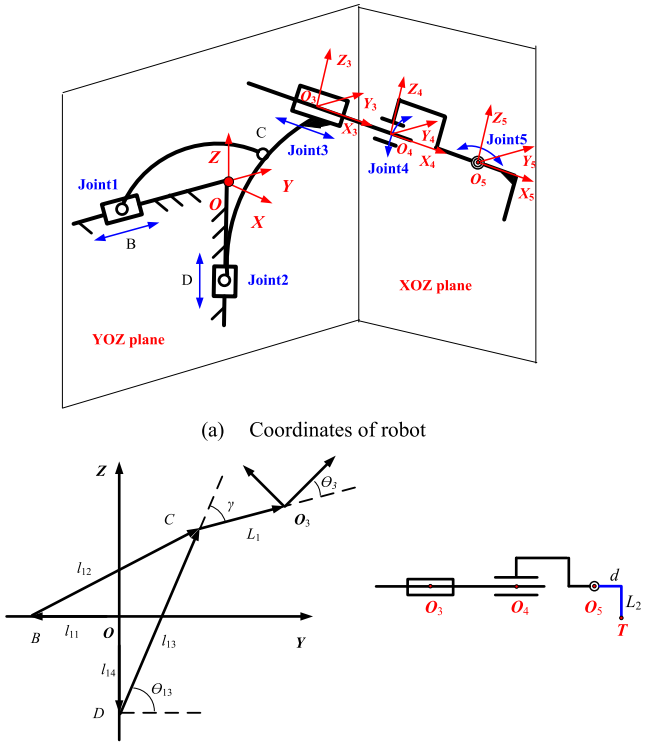

(a) Coordinates of robot

(b) yoz plane (c) xoz plane

FIGURE 4. Kinematic coordinate systems of the improved hybrid robot.

rotational motion. It is noticed that k-wire placement is not the core content in this paper. Therefore, the last joint would not be considered in the following content.

2) KINEMATIC MODEL

Kinematic model establishes the relation between joint variables and tool position. The coordinate systems of robot are established as shown in figure 4. The $\boldsymbol{O}$ coordinate, $\boldsymbol{O_3}$ coordinate, $\boldsymbol{O_4}$ coordinate and $\boldsymbol{O_5}$ coordinate represent the base coordinate, joint 3 coordinate, joint 4 coordinate and joint 5coordinate respectively. Joint 1, joint 2 and joint 3 move along $\boldsymbol{O}$-$\boldsymbol{y}$ axis, $\boldsymbol{O}$-$\boldsymbol{z}$ axis and $\boldsymbol{O}$-$\boldsymbol{x}$ axis respectively. Joint 4 and joint 5 rotate around $\boldsymbol{O}_3$-$\boldsymbol{x}$ axis and $\boldsymbol{O}_4$-$\boldsymbol{y}$ axis respectively. It is

TABLE 2. Structure parameters of robot.

Parameters	Definition
l_{12}	Distance between B and C
l_{13}	Distance between D and C
L_1	Distance between origin of $\boldsymbol{O}_3$ and C
γ	Angle between link DC and link CO_3
θ	Angle between link L_1 and $\boldsymbol{O}_3$-y at the initial position of robot
d, L_2	Tool structure parameters

TABLE 3. Joint variables of robot.

Variables	l_{11}	l_{14}	l_3	θ_4	θ_5
Definition	Joint 1	Joint 2	Joint 3	Joint 4	Joint 5

noticed that the kinematic solution in this paper is similar to the content proposed in [31], however the process of kinematic calculation is different from the former content due to position variations between $\boldsymbol{O_3}$ coordinate and $\boldsymbol{O_4}$ coordinate. To describe the kinematic model of robot more clearly, the definition of structure parameters and joint variables are listed in table 2 and table 3 respectively.

In figure 4(b), B, C, and D could be represented respectively as $B(-l_{11}, 0)$, $C(y_c, z_c)$, $D(0, -l_{14})$. The kinematic model of the first two joints could be obtained as below

$$\begin{cases} (y_c + l_{11})^2 + z_c^2 = l_{12}^2 \\ y_c^2 + (z_c + l_{14})^2 = l_{13}^2 \end{cases} \tag{1}$$

(y_c, z_c) could be described as:

$$\begin{cases} y_c = l_{13} \cdot \cos(\theta_{13}) \\ z_c = l_{13} \cdot \sin(\theta_{13}) - l_{14} \end{cases} \tag{2}$$

where θ_{13} represents the angle between link CD and $\boldsymbol{O}$-$\boldsymbol{y}$ axis. And the position of $\boldsymbol{O}_3$ in $\boldsymbol{O}$ coordinate could be computed using (1) and (2) as:

$$\begin{cases} x_{O_3} = l_3 \\ y_{O_3} = y_c + L_1 \cos(\theta_{13} + \gamma) \\ z_{O_3} = z_c + L_1 \sin(\theta_{13} + \gamma) \end{cases} \tag{3}$$

The angle θ_3 of $\boldsymbol{O}_3$ coordinate around $\boldsymbol{O}$-$\boldsymbol{x}$ is influenced by the first two joints and could be computed as:

$$\theta_3 = \theta_{13} + \gamma + \theta \tag{4}$$

Next, the transformation matrix $\boldsymbol{T}_{\boldsymbol{O}_3}^{\boldsymbol{O}}$ between $\boldsymbol{O}_3$ coordinate and $\boldsymbol{O}$ coordinate could be described based on (3) and (4) as:

$$\boldsymbol{T}_{\boldsymbol{O}_3}^{\boldsymbol{O}} = \begin{bmatrix} 1 & 0 & 0 & x_{O_3} \\ 0 & \cos(\theta_3) & -\sin(\theta_3) & y_{O_3} \\ 0 & \sin(\theta_3) & \cos(\theta_3) & z_{O_3} \\ 0 & 0 & 0 & 1 \end{bmatrix} \tag{5}$$

Then, the transformation matrix $\boldsymbol{T}_{\boldsymbol{O}_4}^{\boldsymbol{O}_3}$ between $\boldsymbol{O}_4$ coordinate and $\boldsymbol{O}_3$ coordinate could be represented as:

$$\boldsymbol{T}_{\boldsymbol{O}_4}^{\boldsymbol{O}_3} = \begin{bmatrix} 1 & 0 & 0 & 0 \\ 0 & \cos\theta_4 & -\sin\theta_4 & 0 \\ 0 & \sin\theta_4 & \cos\theta_4 & 0 \\ 0 & 0 & 0 & 1 \end{bmatrix} \tag{6}$$

In similar way, the transformation matrix $T_{O_5}^{O_4}$ could be represented as:

$$\boldsymbol{T}_{\boldsymbol{O}_5}^{\boldsymbol{O}_4} = \begin{bmatrix} \cos(-\theta_5) & 0 & \sin(-\theta_5) & 0 \\ 0 & 1 & 0 & 0 \\ -\sin(-\theta_5) & 0 & \cos(-\theta_5) & 0 \\ 0 & 0 & 0 & 1 \end{bmatrix} \tag{7}$$

In addition, the coordinate $\boldsymbol{P}_{\boldsymbol{tool}}^{\boldsymbol{O}_5}$ of tool in joint 5 coordinate could be obtained as:

$$\boldsymbol{P}_{\boldsymbol{tool}}^{\boldsymbol{O}_5} = \begin{bmatrix} d & 0 & -L_2 & 1 \end{bmatrix}^{\mathrm{T}} \tag{8}$$

Therefore, the coordinate $\boldsymbol{P}_{\boldsymbol{tool}}^{\boldsymbol{O}}$ of tool in base coordinate of robot could be obtained by (5) to (8) and expressed as:

$$\boldsymbol{P}_{\boldsymbol{tool}}^{\boldsymbol{O}} = \begin{bmatrix} x & y & z & 1 \end{bmatrix}^{\mathrm{T}} = \boldsymbol{T}_{\boldsymbol{O}_3}^{\boldsymbol{O}} \cdot \boldsymbol{T}_{\boldsymbol{O}_4}^{\boldsymbol{O}_3} \cdot \boldsymbol{T}_{\boldsymbol{O}_5}^{\boldsymbol{O}_4} \cdot \boldsymbol{P}_{tool}^{\boldsymbol{O}_5} \tag{9}$$

Forward kinematic solves the pose (position and orientation) of tool in base coordinate of robot based on the structural parameters and joint variables. The mathematical model could be expressed as (10) with the help of (4) and (9).

$$\begin{cases} x = l_3 + d \cdot \cos(\theta_5) + L_2 \cdot \sin(\theta_5) \\ y = -(d \cdot \sin(\theta_5) - L_2 \cdot \cos(\theta_5)) \cdot \sin(\theta_x) + y_c \\ \quad +L_1 \cos(\theta_{13} + \gamma) \\ z = (d \cdot \sin(\theta_5) - L_2 \cdot \cos(\theta_5)) \cdot \cos(\theta_x) + z_c \\ \quad +L_1 \cdot \sin(\theta_{13} + \gamma) \\ \theta_x = \theta_{13} + \gamma + \theta + \theta_4 \\ \theta_y = -\theta_5 \end{cases} \tag{10}$$

Inverse kinematic solves joint variables according to the pose of tool and structural parameters. The mathematical model could be expressed as (11) based on (1) to (10).

$$\begin{cases} l_{11} = \dfrac{-2y_c + \sqrt{4y_c^2 - 4(y_c^2 + z_c^2 - l_{12}^2)}}{2} \\ l_{14} = l_{13} \cdot \sin(\theta_{13}) - z_c \\ l_3 = x - d \cdot \cos(\theta_5) - L_2 \cdot \sin(\theta_5) \\ \theta_4 = \theta_x - \theta_{13} - \gamma - \theta \\ \theta_5 = -\theta_y \end{cases} \tag{11}$$

3) JACOBIAN MATRIX

Jacobian matrix could obtain the tool velocity based on joint velocity. The tool velocity could be represented as:

$$\dot{\boldsymbol{X}} = [\dot{x}, \dot{y}, \dot{z}, \dot{\theta}_x, \dot{\theta}_y]^{\mathrm{T}} \tag{12}$$

The joint velocity could be represented as:

$$\dot{\boldsymbol{q}} = [\dot{l}_{11}, \dot{l}_{14}, \dot{l}_3, \dot{\theta}_4, \dot{\theta}_5] \tag{13}$$

Then, the mapping model from joint to tool could be expressed as:

$$\dot{\boldsymbol{X}} = \frac{d\boldsymbol{X}}{d\boldsymbol{q}} \cdot \frac{d\boldsymbol{q}}{t} = \frac{d\boldsymbol{X}}{d\boldsymbol{q}} \cdot \dot{\boldsymbol{q}} = \boldsymbol{J} \cdot \dot{\boldsymbol{q}} \tag{14}$$

where

$$\boldsymbol{J} = \begin{bmatrix} \frac{\partial x}{\partial l_{11}} & \frac{\partial x}{\partial l_{14}} & \frac{\partial x}{\partial l_3} & \frac{\partial x}{\partial \theta_4} & \frac{\partial x}{\partial \theta_5} \\ \frac{\partial y}{\partial l_{11}} & \frac{\partial y}{\partial l_{14}} & \frac{\partial y}{\partial l_3} & \frac{\partial y}{\partial \theta_4} & \frac{\partial y}{\partial \theta_5} \\ \frac{\partial z}{\partial l_{11}} & \frac{\partial z}{\partial l_{14}} & \frac{\partial z}{\partial l_3} & \frac{\partial z}{\partial \theta_4} & \frac{\partial z}{\partial \theta_5} \\ \frac{\partial \theta_x}{\partial l_{11}} & \frac{\partial \theta_x}{\partial l_{14}} & \frac{\partial \theta_x}{\partial l_3} & \frac{\partial \theta_x}{\partial \theta_4} & \frac{\partial \theta_x}{\partial \theta_5} \\ \frac{\partial \theta_y}{\partial l_{11}} & \frac{\partial \theta_y}{\partial l_{14}} & \frac{\partial \theta_y}{\partial l_3} & \frac{\partial \theta_y}{\partial \theta_4} & \frac{\partial \theta_y}{\partial \theta_5} \end{bmatrix}$$

Inverse jacobian matrix could acquire the joint velocity driving the robot by tool velocity. Unfortunately, inverse jacobian matrix is difficult to solve directly by the way of inverse matrix. We calculate inverse jacobian matrix in term of definition and the corresponding equation could be represented as:

$$\boldsymbol{J}^{-1} = \begin{bmatrix} 0 & N_{12} & N_{13} & N_{14} & N_{15} \\ 0 & N_{22} & -1 & N_{24} & N_{25} \\ 1 & 0 & 0 & 0 & g_{11} \\ 0 & \dfrac{2g_2}{g_8} & 0 & \dfrac{2g_7}{g_8} + 1 & \dfrac{2g_9}{g_8} \\ 0 & 0 & 0 & 0 & -1 \end{bmatrix} \tag{15}$$

The details about $\boldsymbol{J}$ and $\boldsymbol{J}^{-1}$ are described in appendix A and B respectively.

B. HUMAN-ROBOT COOPERATION

During the process of image acquisition, it is difficult to display all the circular control points on the image based on the bi-planar position given in software. In addition, tool may interfere with the patient during the process of positioning. Fortunately, human-robot cooperation could solve the two problems above.

A six dimensional force transducer (ATI mini 45) installed on the joint 5 is used to measure the magnitude and direction of the force and torque exerted by operator during human-robot cooperation. However, the load after force transducer would seriously affect the identification of operator intention and need to be compensated. In addition, fuzzy inference system is applied in human-robot cooperation to estimate the intention of operator [35]. It is noticed that position drag and orientation drag in robotic system are

implemented separately based on a button near the transducer to make better experience for operator.

1) TOOL WEIGHT COMPENSATION

The influence of tool weight for force and torque exerted by operator would be compensated respectively. The former is based on mathematical model while the latter is based on data fitting. First, we transfer the values measured in transducer coordinate into joint 5 coordinate based on the mounting position and orientation of transducer. The values in joint 5 coordinate could be represented as

$$\begin{aligned}\boldsymbol{F}_{Joint5} &= \boldsymbol{T}_{transducer}^{Joint5} \cdot \boldsymbol{F}_{transducer} \\ &= \begin{bmatrix} 0 & -1 & 0 & 0 & 0 & 0 \\ 0 & 0 & -1 & 0 & 0 & 0 \\ 1 & 0 & 0 & 0 & 0 & 0 \\ 0 & 0 & 0 & 0 & -1 & 0 \\ 0 & 0 & 0 & 0 & 0 & -1 \\ 0 & 0 & 0 & 1 & 0 & 0 \end{bmatrix} \begin{bmatrix} f_x \\ f_y \\ f_z \\ t_x \\ t_y \\ t_z \end{bmatrix} \end{aligned} \tag{16}$$

where $\boldsymbol{F}_{Joint5} = [T\_f_x, T\_f_y, T\_f_z, T\_t_x, T\_t_y, T\_t_z]^{\mathrm{T}}$. Next, the tool weight in base coordinate need to be decomposed into joint 5 coordinate based on the matrix between base coordinate and joint 5 coordinate and the weight in joint 5 coordinate could be expressed as

$$\boldsymbol{G}_{Joint5} = \boldsymbol{R}_{\boldsymbol{O}}^{\boldsymbol{O}_5} \cdot \boldsymbol{G}_{base} = \begin{bmatrix} \cos\theta_x \cdot sin\theta_y \cdot g \\ -sin\theta_x \cdot g \\ -\cos\theta_x \cdot \cos\theta_y \cdot g \end{bmatrix} \tag{17}$$

where $\boldsymbol{G}_{Joint5} = \begin{bmatrix} G_{x\_Joint5} & G_{y\_Joint5} & G_{z\_Joint5} \end{bmatrix}^{\mathrm{T}}$, $\boldsymbol{R}_{\boldsymbol{O}}^{\boldsymbol{O}_5}$ represents the orientation part of $\boldsymbol{T}_{\boldsymbol{O}}^{\boldsymbol{O}_5}$. Then, we could obtain the force $\boldsymbol{H}_{Joint5}$ exerted by operator in joint 5 coordinate according to (16) and (17).

$$\begin{aligned}\boldsymbol{H}_{Joint5} &= \begin{bmatrix} H_x \\ H_y \\ H_z \end{bmatrix} = \begin{bmatrix} T\_f_x \\ T\_f_y \\ T\_f_z \end{bmatrix} - \left\{ \begin{bmatrix} G_{x\_Joint5} \\ G_{y\_Joint5} \\ G_{z\_Joint5} \end{bmatrix} - \begin{bmatrix} f_{x0} \\ f_{y0} \\ f_{z0} \end{bmatrix} \right\} \\ &= \begin{bmatrix} T\_f_x - 30 \cdot \cos(\theta_x) \cdot \sin(\theta_y) \\ T\_f_y + 30 \cdot \sin(\theta_x) \\ T\_f_z + 30 \cdot \cos(\theta_x) \cdot \cos(\theta_y) - 30 \end{bmatrix} \end{aligned} \tag{18}$$

where $f_{x0} = 0$, $f_{y0} = 0$, $f_{z0} = -30$. Finally, the force $\boldsymbol{H}_{base}$ unaffected by tool weight in base coordinate could be computed by $\boldsymbol{H}_{Joint5}$ and $\boldsymbol{R}_{\boldsymbol{O}_5}^{\boldsymbol{O}}$ and expressed as:

$$\begin{aligned}&\boldsymbol{H}_{base} \\ &= \boldsymbol{R}_{\boldsymbol{O}_5}^{\boldsymbol{O}} \cdot \boldsymbol{H}_{Joint5} \\ &= \begin{bmatrix} \cos\theta_y \cdot H_x + \sin\theta_y \cdot H_z \\ \sin\theta_x \cdot \sin\theta_y H_x + \cos\theta_x \cdot H_y - \sin\theta_x \cdot \cos\theta_y \cdot H_z \\ -\cos\theta_x \cdot \sin\theta_y \cdot H_x + \sin\theta_x \cdot H_y + \cos\theta_x \cdot \cos\theta_y \cdot H_z \end{bmatrix} \end{aligned} \tag{19}$$

where $\boldsymbol{R}_{\boldsymbol{O}_5}^{\boldsymbol{O}} = \boldsymbol{R}_{\boldsymbol{O}}^{\boldsymbol{O}_5^{\mathrm{T}}} = \boldsymbol{R}_{\boldsymbol{O}}^{\boldsymbol{O}_5^{-1}}$

$\boldsymbol{H}_{base}$ would be set as the input force signal for identification of operator intention. In addition, we also need to compensate the influence of tool weight for torque exerted by operator based on polynomial fitting method. First, we drive joint 4 and joint 5 in joint space. Then, we measure torques around three axes and record the θ_x and joint 5 variables. The polynomial fitting is a widely used fitting method. The torque around each axis is selceted as output and the θ_x and joint 5 are selected as input. Equations (20), (21), and (22) are obtained based on matlab sftool toolbox. The degree of polynomial fitting formulas is selected according to fitting error. Finally, torque around each axis could be represented by θ_x and joint 5 as:

$$\begin{aligned}\Delta T_x = {} & 6.945 - 35.98 \cdot \theta_x + 32.32 \cdot \theta_5 - 0.001347 \cdot \theta_x^2 \\ & - 0.006577 \cdot \theta_x \cdot \theta_5 - 0.007828 \cdot \theta_5^2 + 0.001725 \cdot \theta_x^3 \\ & - 0.00412 \cdot \theta_x^2 \cdot \theta_5 + 5.266 \cdot 10^{-6} \cdot \theta_x \cdot \theta_5^2 \\ & - 0.001286 \cdot \theta_5^3 \end{aligned} \tag{20}$$

$$\begin{aligned}\Delta T_y = {} & -77.1 - 13.52 \cdot \theta_x - 0.03748 \cdot \theta_5 - 0.2096 \cdot \theta_x^2 \\ & - 0.001301 \cdot \theta_x \cdot \theta_5 - 0.2228 \cdot \theta_5^2 + 0.0006763 \cdot \theta_x^3 \\ & - 1.077 \cdot 10^{-5} \cdot \theta_x^2 \cdot \theta_5 + 8.217 \cdot 10^{-5} \cdot \theta_x \cdot \theta_5^2 \\ & - 5.86 \cdot 10^{-5} \cdot \theta_5^3 \end{aligned} \tag{21}$$

$$\begin{aligned}\Delta T_z = {} & 40.66 - 0.2027 \cdot \theta_x + 12.29 \cdot \theta_5 + 0.3109 \cdot \theta_x^2 \\ & - 0.004489 \cdot \theta_x \cdot \theta_5 + 0.3013 \cdot \theta_5^2 + 0.0003569 \cdot \theta_x^3 \\ & - 0.001594 \cdot \theta_x^2 \cdot \theta_5 - 5.961 \cdot 10^{-5} \cdot \theta_x \cdot \theta_5^2 \\ & - 0.0006359 \cdot \theta_5^3 - 9.58 \cdot 10^{-6} \cdot \theta_x^4 + 1.15 \cdot 10^{-6} \cdot \theta_x^3 \\ & \cdot \theta_5 - 3.946 \cdot \theta_x^2 \cdot \theta_5^2 - 1.005 \cdot 10^{-6} \cdot \theta_x \cdot \theta_5^3 \\ & - 5.059 \cdot 10^{-6} \cdot \theta_5^4 \end{aligned} \tag{22}$$

Equations (20), (21), and (22) need to be transferred into joint coordinate based on (16) to help identify operator intention. It is noting that position drag is implemented in base coordinate and orientation drag is realized in joint coordinate.

2) FUZZY VARIABLE ADMITTANCE CONTROLLER

Admittance controller is widely applied in human-robot cooperation [32]. However, constant admittance controller could not balance the positioning precision of tool and energy exerted by operator. Lecours *et al.* [33] presented a variable admittance controller by the direction of desired acceleration and velocity. But the damping ratio is difficult to be acquired in practical applications. Corteville *et al.* [34] proposed a assistance parameter to help operator move the load. However, the jerk trajectory depending on initial position, final position and duration of movement need to be given before motion. Duchaine *et al.* [56] estimated human intentions according to differentiation of the force. However, a decrease in the magnitude of the force does not indicate a deceleration intention. In addition, the stability of the robot would be influenced by arm stiffness [57]. Therefore, we proposed a fuzzy variable admittance controller based on stiffness identification of human arm to realize human-robot cooperation [35]. The block diagram of fuzzy variable admittance controller is shown in figure 5.

In figure 5, the force exerted by operator is derived from transducer values without the influence of tool weight and computed by the previous section, the max damping in

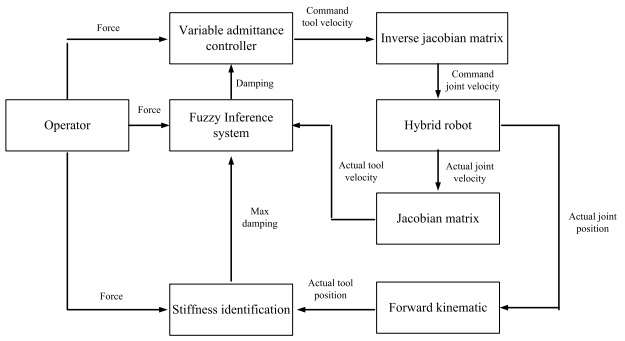

FIGURE 5. Human-robot cooperation based on fuzzy variable admittance controller.

admittance controler is decided by the stiffness of human arm estimated by the recursive least square, the damping in admittance controller is computed by fuzzy inference system considering the max damping, the hybrid robot in the velocity loop is driven based on admittance controller with variable damping to follow the operator intention.

C. INTRAOPERATIVE NAVIGATION BASED ON BI-PLANAR

1) BI-PLANAR DESIGN

Bi-planar made of acrylic sheets is the core module for navigation. For computer-assisted surgery, there are usually two types calibration cages which are used to obtain mapping model from image coordinate to space coordinate. One is attached to image intensifier of C-arm [42]–[46], the other is placed next to the patient [47], [48]. The former usually has two layers on which a series fiducials are arranged, and could be divided into one piece [42]–[45] and two pieces [46]. The fluoroscopy images would be contaminated by shadows of metal spheres in one piece structure. Two pieces could overcome the problem mentioned above [46]. however, both one piece and two pieces are designed for computer-assisted navigation system, and could not be directly applied in robot-assisted system. In addition, it is noticed that the structure of calibration cage would be determined by image intensifier of C-arm and this limits the application in surgery due to the different C-arms in hospitals. The latter usually has a free-moving calibration object which could match different C-arms. In [47] and [48], the calibration object is fixed to the patient' s upper body using a conventional belt. However, this fixed method is not reliable in clinic. Furthermore, the target path and fiducials could not be displayed on lateral fluoroscopy image at the same time. Therefore, a novel bi-planar which is fixed on the end of robot is designed and the following features are considered.

- The number of steel balls on each plane should be as many as possible to ensure the precision.
- Target path could be displayed on fluoroscopy images without circular control point interference.
- The distribution area of steel balls should be as large as possible, but should satisfy C-arm imaging range.

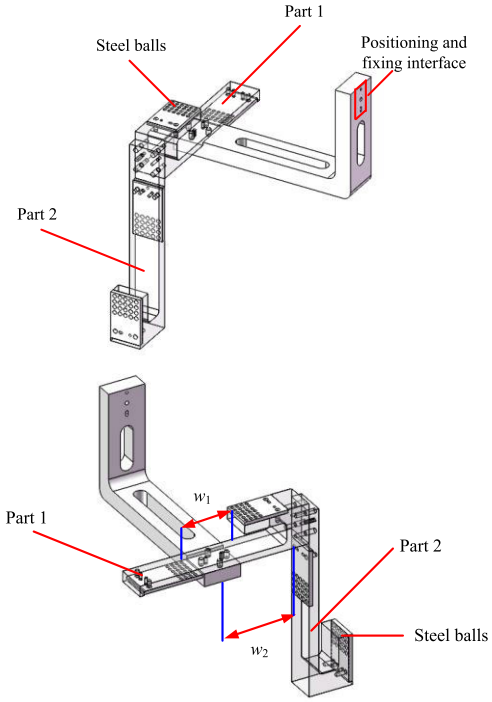

FIGURE 6. The structure of bi-planar.

- Structure of bi-planar should be as compact as possible, but cannot interfere with the patient.
- The bi-planar could be quickly installed and removed from the end of robot.

According to the features above, we design structure of bi-planar as shown in figure 6. Both part 1 and part 2 have two layers of plane on which a series of 4 mm diameter steel balls are arranged and the distance between adjacent steel balls is 6 mm. In order to ensure the precision, the quantity and distribution of steel balls have been as large as possible within the imaging range. The positioning and fixing interface connected to the end of robot could realize the fast installation and disassembly. In addition, the parameter w1, which is set to 64 mm, could avoid blocking the target path in fluoroscopy image and the parameter w2, which is set to 165 mm, could avoid interfering with the patient. Therefore, bi-planar designed in this paper could meet the demands for navigation.

2) DISTORTION CORRECTION

The images derived from C-arm are usually affected by distortion which is dependent on curvature of its phosphorous panel and its surrounding electro-magnetic field [36]. Therefore, distortion correction of fluoroscopy image is necessary process in robotic system. In terms of the models adopted in distortion correction, the methods could be categorized as the global correction method [37] and the local correction method [38]. For the global method, the distortion over the whole image is considered as the continuous and could be modeled by polynomial. However, global method cannot

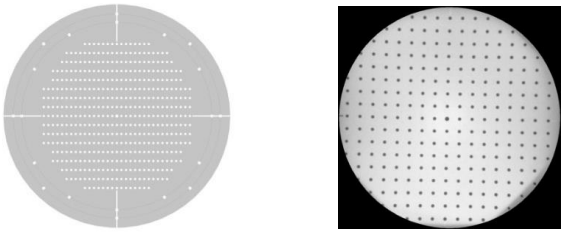

(a) Calibration plate made of acrylic sheets

(b) Fluoroscopy image of calibration plate

FIGURE 7. Calibration plate for image correction.

correct the local distortion. Local correction method could make up for the shortcomings of global methods, and has better accuracy. Therefore, local correction method is applied in this paper.

The procedure of image correction consists of ideal control point creation, mapping from ideal control points to real control points, and interpolation of gray value. First, the calibration plate is designed as shown in figure 7(a) and attached to the intensifier of C-arm. Next the fluoroscopy image with control points is acquired as shown in figure 7(b). Then, the real control points would be extracted from fluoroscopy image and the ideal control points could be obtained by interpolation using the points in the center region of fluoroscopy image. In addition, the mapping matrix from ideal control points to real control points is computed by local correction method. Finally, the gray value over the whole image corrected could be computed by interpolation.

3) CIRCULAR CONTROL POINT DETECTION

To promote the use of robotic system in orthopaedic operating room, the operation procedure should be as simple as possible. Therefore, circular control point detection for extracting location of steel balls on bi-planar fluoroscopy image should be realized automatically. There are two core problems need to be considered to meet the demand mentioned, one is the interference of strong background, the other is the variations of position, size, and gray value of control points. We proposed an effective detector named as HVCD which could detect Multi-Circle on synthetic and natural images [39]. However, it could not afford the case of minor-radius. Then, we proposed a robust circular control point detector consisting of SVM, IHVCD, and distance & density clustering algorithm, for bi-planar spine surgery navigation system [40]. The workflow of detector is shown in figure 8.

SVM in detector could improve the detection efficiency by ignoring the most regions which consist of real control points and false control points and need not to be further processed. IHVCD in detector could ensure detection accuracy based on extracting valid control points from possible control points. The distance & density clustering algorithm could realize large robustness by removing the ineffective control points from valid control points. This detector could meet the demands of control point detection on spine model bone, swine bone, and swine according to the experiments.

4) TARGET PATH CALCULATION

For navigation applied in this paper, the transformation of target path from the image coordinate to base coordinate of robot is the main task. This transformation matrix could be expressed as:

$$\boldsymbol{T}_{path}^{robot\_base} = \boldsymbol{T}_{bi-planar}^{robot\_base} \cdot \boldsymbol{T}_{image}^{bi-planar} \cdot \boldsymbol{T}_{path}^{image} \tag{23}$$

where $\boldsymbol{T}_{bi-planar}^{robot\_base}$ represents the transformation matrix of bi-planar coordinate with respect to base coordinate of robot and could be obtained by forward kinematic of robot, $\boldsymbol{T}_{path}^{image}$ represents the pose of target path in image coordinate and could be obtained by path planning, $\boldsymbol{T}_{image}^{bi-planar}$ represents the transformation matrix of image coordinate with respect to bi-planar coordinate and could be computed by registration.

In fact, $\boldsymbol{T}_{image}^{bi-planar}$ could be obtained by two methods consisting of 3D-2D registration and 2D-2D registration [41]. 3D-2D registration refers to the pin-hole camera model which could map 3D target path in bi-planar coordinate into 2D target paths in ap and lateral image coordinates or compute the 3D target path in bi-planar coordinate by 2D target paths in ap and the lateral image coordinates. However, 2D-2D registration mainly obtains the transformation matrix between image coordinate and each plane coordinate of bi-planar, and could only realize the mapping from 2D target paths in fluoroscopy image coordinates to 3D target path in bi-planar coordinate. Considering that 2D-2D registration is more accurate than 3D-2D registration from image coordinate to space coordinate. Therefore, 2D-2D registration is adopted in this paper and bi-planar navigation method is described in figure 9.

Transformation matrix between each plane coordinate of bi-planar and fluoroscopy image coordinate could be computed by registration between the control points detected on fluoroscopy image and the corresponding steel balls attached on bi-planar. In figure 9, blue lines represent planes on which steel balls are distributed, P11, P12, P21, and P22 could be obtained by transferring input 1 and input 2 on ap fluoroscopy image into plane1 and plane 2 using registration results. In the same way, P31, P32, P41, and P42 could be acquired. In this way, input 1 in bi-planar coordinate could be obtained by P11, P21, P31, and P41. The other target points input 2, output 1, and output 2 could also be acquired in the similar method.

5) TOOL POSITIONING

The precision of robotic system is the most important performance for spine surgery. Traditional kinematic control is usually implemented in the base coordinate of robot and this mode is considered as the open loop. The precision of kinematic control is determined by the absolute positioning accuracy of robot which is difficult to be guaranteed. Therefore, we select 3D optical positioner to measure the relative pose errors between real tool and target path and the errors

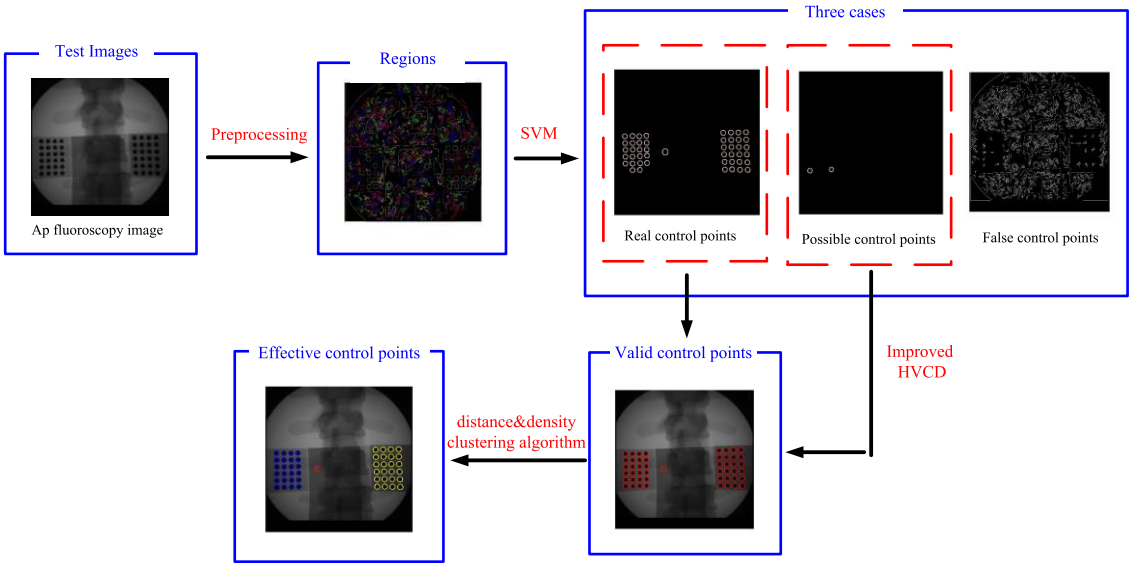

FIGURE 8. Workflow of circular control point detector.

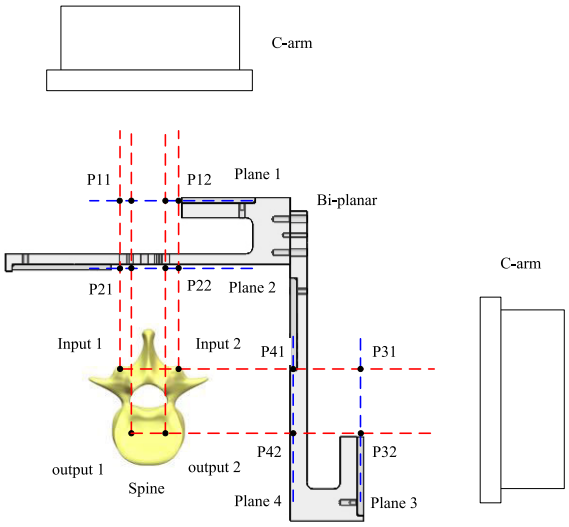

FIGURE 9. Bi-planar navigation method.

would be sent to robot to realize closed-loop control which would help improve the precision of robotic system. The path after compensation in base coordinate of robot could be represented as:

$$\begin{aligned} &\boldsymbol{T}^{robot\_base}_{path\_compensation} \\ &= \boldsymbol{T}^{robot\_base}_{path} \cdot \Delta \boldsymbol{T}_{error} \\ &= \boldsymbol{T}^{robot\_base}_{path} \cdot (\boldsymbol{T}^{mark\_patient}_{tool\_real})^{-1} \cdot T^{mark\_patient}_{path} \\ &= \boldsymbol{T}^{robot\_base}_{path} \cdot (\boldsymbol{T}^{mark\_patient}_{ndi} \cdot \boldsymbol{T}^{ndi}_{mark\_robot} \cdot \boldsymbol{T}^{mark\_robot}_{tool\_real})^{-1} \\ &\quad \cdot (\boldsymbol{T}^{mark\_patient}_{bi-planar} \cdot \boldsymbol{T}^{bi-planar}_{image} \cdot \boldsymbol{T}^{image}_{path}) \end{aligned} \tag{24}$$

where $\boldsymbol{T}^{mark\_robot}_{tool\_real}$ represents the transformation matrix of tool coordinate with respect to mark_robot coordinate, $\boldsymbol{T}^{ndi}_{mark\_robot}$ represents the transformation matrix of mark_robot coordinate with respect to ndi coordinate, $\boldsymbol{T}^{mark\_patient}_{ndi}$ represents the transformation matrix of ndi coordinate with respect to mark_patient coordinate, $\boldsymbol{T}^{mark\_patient}_{bi-planar}$ represents the transformation matrix of bi-planar coordinate with respect to mark_patient coordinate and could be obtained by calibration. $\boldsymbol{T}^{mark\_patient}_{tool\_real}$ represents the transformation matrix of real pose of tool with respect to mark_patient coordinate. $\boldsymbol{T}^{mark\_patient}_{path}$ represents the transformation matrix of the pose of target path with respect to mark_patient coordinate. The process above could be described in figure 10. The blue lines represent the real pose of tool in mark_patient coordinate, black line represents the target path in mark_patient coordinate, green line represents the target path in robot_base coordinate, and yellow line represents pose error $\Delta \boldsymbol{T}_{error}$.

TABLE 4. Ideal distance in robot base coordinate.

Index	Position 1	Position 2	Ieal distance
1	(550,350,-70)	(550,400,-70)	50
2	(550,400,-70)	(550,450,-70)	50
3	(550,450,-70)	(550,500,-70)	50
4	(550,500,-70)	(550,550,-70)	50
5	(550,550,-70)	(550,600,-70)	50
6	(550,600,-70)	(550,600,-20)	50
7	(550,600,-20)	(600,600,-20)	50
8	(600,600,-20)	(650,600,-20)	50
9	(650,600,-20)	(650,600,-100)	80
10	(650,600,-100)	(680,600,-150)	58.31
11	(680,600,-150)	(700,600,-200)	53.85
12	(700,600,-200)	(700,550,-250)	70.71
13	(700,550,-250)	(660,500,-100)	163.09
14	(660,500,-100)	(700,520,-130)	53.85

III. EXPERIMENTS

In this section, the experiments related to kinematic model of hybrid robot and tool weight compensation are implemented.

TABLE 5. Real distance in laser tracker coordinate.

index	Position 1	Position 2	Real distance
1	(517.03, 1646.61, -100.01)	(554.19, 1680.15, -99.64)	50.06
2	(554.19, 1680.15, -99.64)	(591.39, 1713.67, -99.33)	50.07
3	(591.39, 1713.67, -99.33)	(628.63, 1747.16, -99.10)	50.07
4	(628.63, 1747.16, -99.10)	(665.92, 1780.71, -98.99)	50.16
5	(665.92, 1780.71, -98.99)	(703.29, 1814.40, -99.17)	50.32
6	(703.29, 1814.40, -99.17)	(703.63, 1813.84, -49.37)	49.80
7	(703.63, 1813.84, -49.37)	(737.09, 1776.75, -50.31)	49.96
8	(737.09, 1776.75, -50.31)	(770.56, 1739.68, -51.32)	49.95
9	(770.56, 1739.68, -51.32)	(770.07, 1740.65, -131.02)	79.70
10	(770.07, 1740.65, -131.02)	(789.90, 1719.21, -181.51)	58.32
11	(789.91, 1719.21, -181.51)	(803.09, 1705.34, -231.82)	53.82
12	(803.09, 1705.34, -231.82)	(765.84, 1673.17, -281.79)	70.14
13	(765.84, 1673.17, -281.79)	(702.35, 1666.25, -131.33)	163.45
14	(702.35, 1666.25, -131.33)	(743.89, 1650.58, -162.03)	53.98

TABLE 6. Errors of hybrid robot kinematic model.

Index	1	2	3	4	5	6	7
Error (mm)	0.06	0.07	0.07	0.16	0.32	0.2	0.04
Index	8	9	10	11	12	13	14
Error (mm)	0.05	0.30	0.01	0.03	0.57	0.36	0.13
Average error (mm)				0.17			

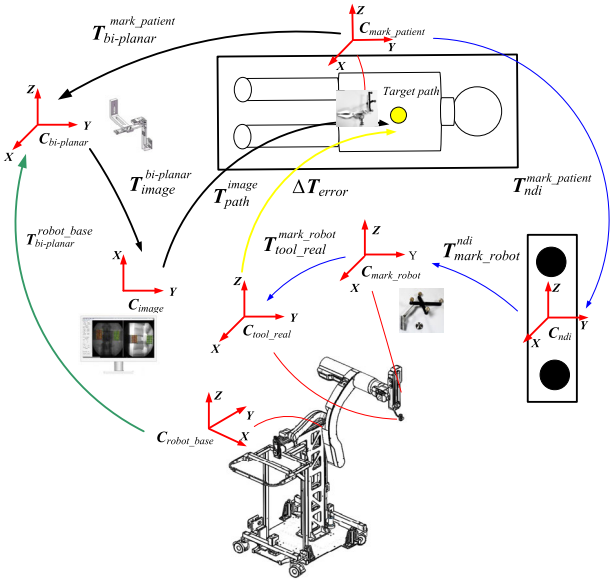

FIGURE 10. Tool positioning with closed-loop control.

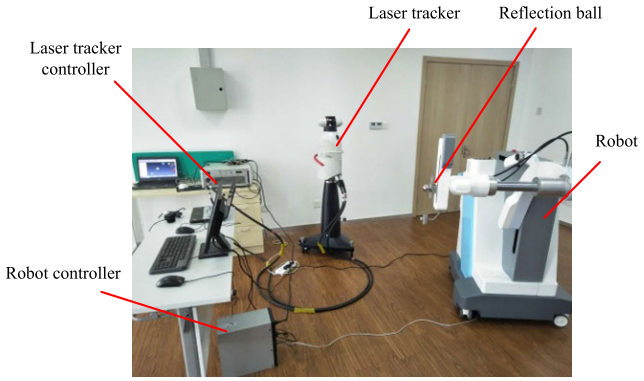

FIGURE 11. Experiment of hybrid robot kinematic model.

In addition, to validate effectiveness of robotic system proposed in this paper, we implement robot-assisted spine surgery experiments in which both the spine model bone and cadaver are conducted.

A. EXPERIMENT OF HYBRID ROBOT KINEMATIC MODEL

If the base coordinate of robot could be easily established by laser tracker, the validation process of kinematic model should be made in base coordinate of robot in normal condition. However, the base coordinate of hybrid robot proposed in this paper could not be obtained directly from laser tracker. Therefore, we select distance between two target positions as the performance to verify the kinematic model. In this way, we do not need to care about which coordinate the data are measured by laser tracker in.

In figure 11, hybrid robot and Leica AT901 laser tracker would be driven by the corresponding controllers respectively. Laser tracker could realize the 10 μm measurement precision. The reflection ball is installed on the end of robot. During this experiment, robot would be driven with the fixed orientation in the base coordinate of robot and the tool position derived from forward kinematic would be recorded as the ideal data. At the same time, the reflection ball position in coordinate of laser tracker would be recorded as the real data. In addition, the performance of distance could be obtained by two adjacent positions. It is noticed that the range of motion in this experiment is 550 mm to 700 mm

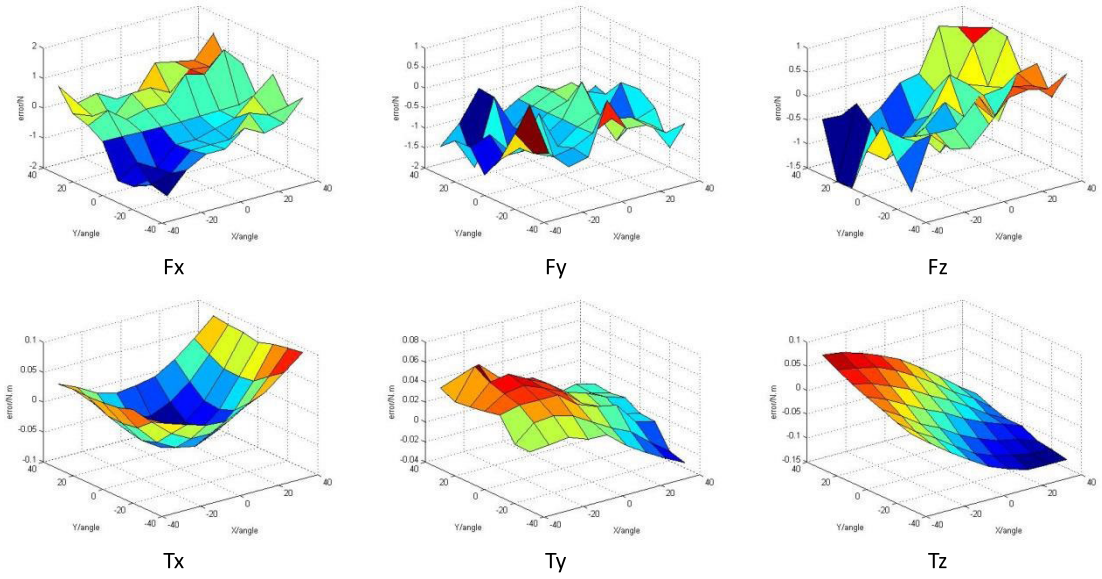

FIGURE 12. Results of tool weight compensation in different orientations.

TABLE 7. Errors of tool weight compensation.

force（N）/ torque（N.M）	Error			
	Ratio (larger than1 N or 0.1N.M)	max	min	mean
Fx	0.1270	1.501	0.002	0.5115
Fy	0.1746	1.776	0.047	0.7477
Fz	0.0635	1.496	0.007	0.4430
Tx	0	0.093	0	0.0359
Ty	0	0.064	0	0.0264
Tz	0.206	0.133	0.006	0.0617

along $\boldsymbol{x}$ direction, 350 mm to 600 mm along $\boldsymbol{y}$ direction, and -20 mm to -250 mm along $\boldsymbol{z}$ direction. In this way, we obtain 14 pairs of positions and compute the distance errors. The ideal distance, real distance and distance errors are listed in table 4, 5 and 6. The mean of distance error is 0.17 mm and much smaller than the motion range. The experimental results demonstrate that the kinematic model could be accepted in the robotic system. In fact, the performance of distance could only contain the effect of the first four joints in the hybrid robot. Fortunately, the last joint could be easily joined in kinematic model. In this way, kinematic model could afford the tasks in robotic system.

B. EXPERIMENT OF TOOL WEIGHT COMPENSATION

In this section, we realize the tool weight compensation based on (19), (20), (21) and (22), and the errors after compensation are measured. The input orientation parameters in this experiment are $\theta_x = [-40, -30, \ldots 40]$ and $\theta_5 = [-30, -20, \ldots 30]$. The output parameters are force errors along three axes and torque errors around three axes after compensation. The experimental results are listed in table 7. According to experiments in which different operators try to interact with robot, human cannot accurately feel force less than 1N and torque less than 0.1N.M by hands. Therefore, 1N and 0.1 N.M are selected as the metrics for weight compensation in table 7. Along three axes, the max mean force error is 0.7477 N and less than 1N. Although the max force error is 1.776 N and the max ratio larger than 1 N is 0.1746,

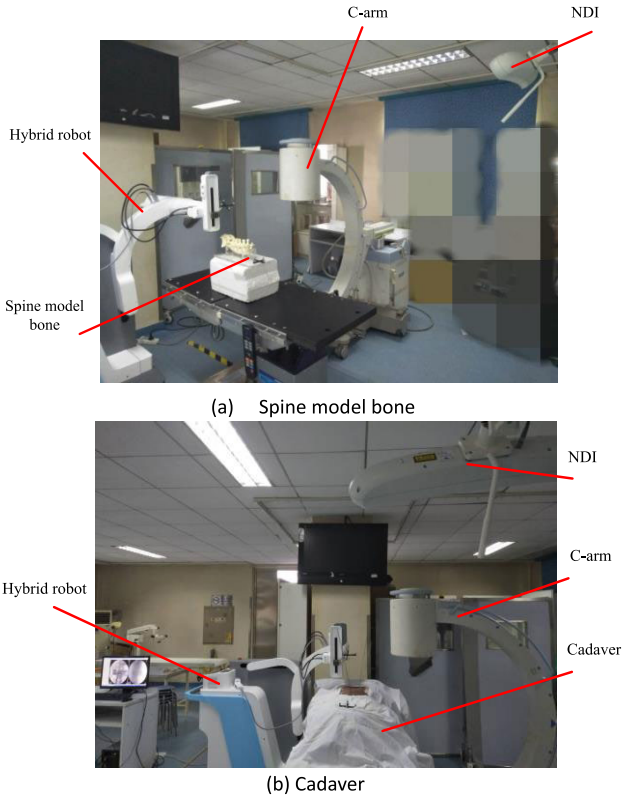

FIGURE 13. Experiments of robot-assisted spine surgery.

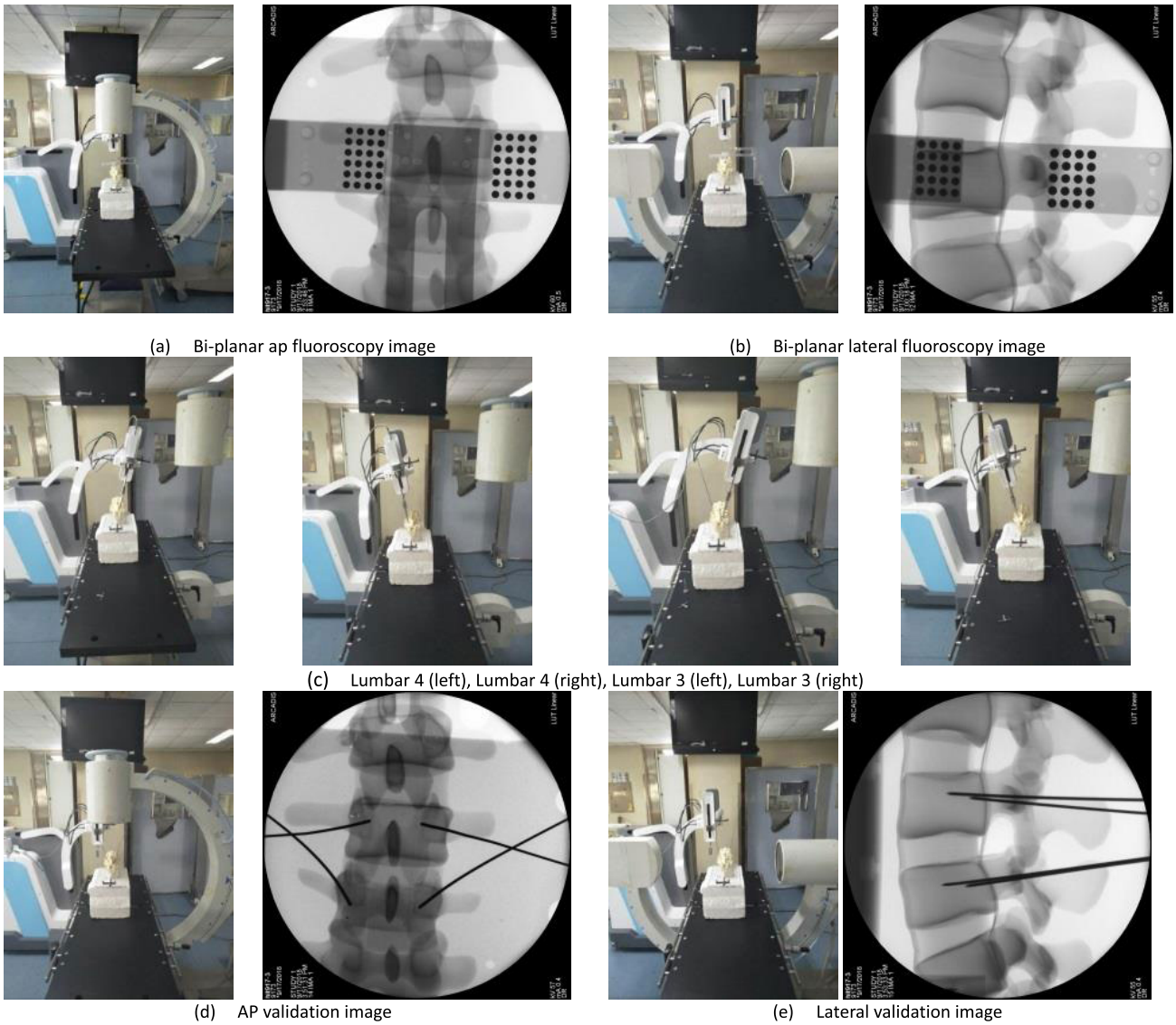

(a) Bi-planar ap fluoroscopy image

(b) Bi-planar lateral fluoroscopy image

(c) Lumbar 4 (left), Lumbar 4 (right), Lumbar 3 (left), Lumbar 3 (right)

(d) AP validation image

(e) Lateral validation image

FIGURE 14. **Experimental results of spine model bone.**

the effect of force error in robotic system could be neglected due to 30N tool weight and 10 N force exerted by operator. The force threshold in human-robot cooperation is set to 1.8N based on the max force error. In similar way, the max mean torque error around x and y axes is 0.0359 N.M and less than 0.1N.M. In addition, the max torque error is 0.093N.M and the max ratio larger than 0.1 N.M is 0. Therefore, the effect of torque error in robotic system could be neglected. The torque threshold in human-robot cooperation is set to 0.1N.M based on the max torque error around x and y axes. It is noticed that torque around z axis would not be applied in human-robot cooperation and the experimental result about z axis would not be discussed in detail. In this way, tool weight compensation could afford task in human-robot cooperation.

To more clearly show the effects of tool weight compensation, we describe force errors along axes and torque errors around axes in figure 12. The horizontal axes represent the input orientation parameters consisting of $\boldsymbol{Y}$ (θ_5) and $\boldsymbol{X}$ (θ_x), and the vertical axis represents the errors after compensation.

Noticed that the experiment of human-robot cooperation based on variable admittance control could be found in [35].

C. EXPERIMENTS OF ROBOT-ASSISTED SPINE SURGERY

To validate the feasibility of robotic system proposed in this paper, we conduct spine model bone experiment and cadaver experiment as shown in figure 13. In two experiments, hybrid robot, C-arm, and 3D optical positioner (NDI Polaris spectra) are adopted and the whole experiments are implemented with the help of surgeons. In addition, the process of experiment follows the procedure described in II.

1) SPINE MODEL BONE EXPERIMENT

We test robotic system on spine model bone. First, ap fluoroscopy image with bi-planar and lateral fluoroscopy image

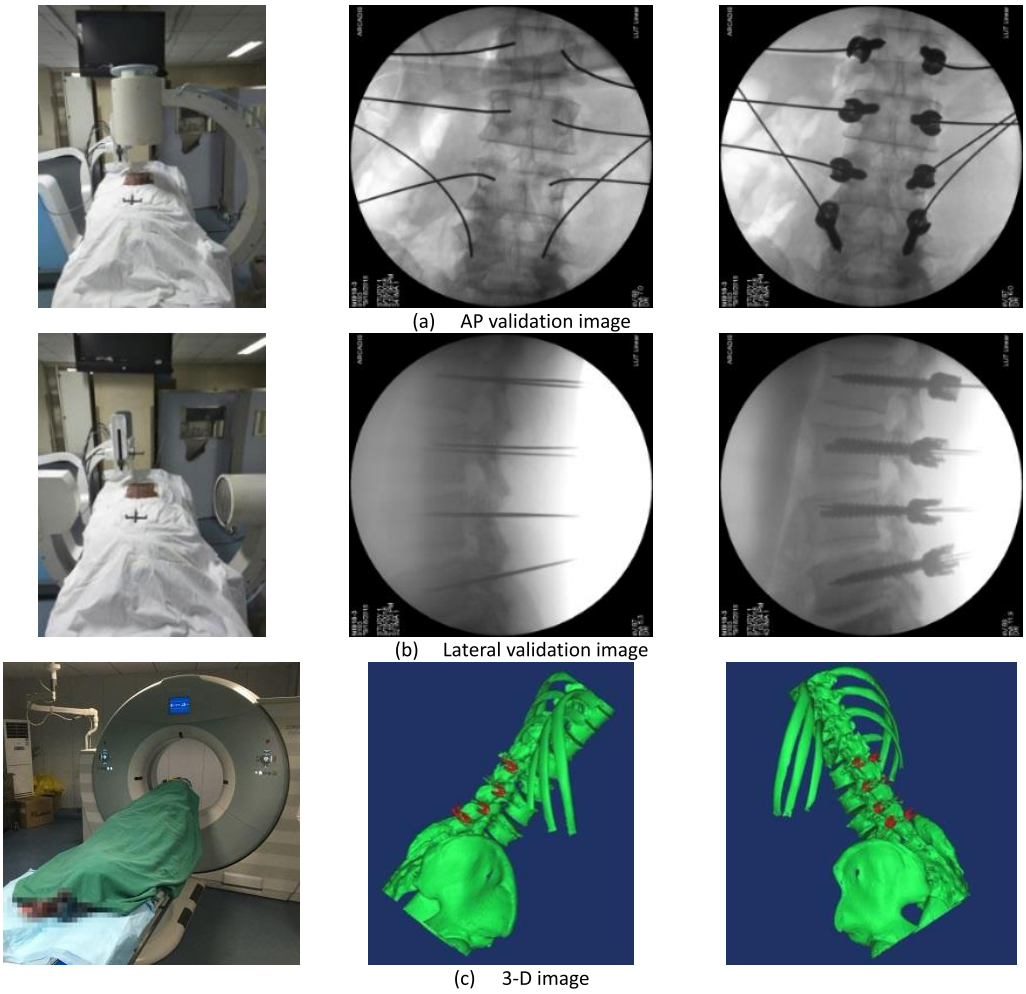

FIGURE 15. Experimental results of cadaver.

with bi-planar would be obtained by C-arm as shown in figure 14(a) and (b), and the position relation between bi-planar, patient and C-arm could be adjusted based on human-robot cooperation. Then, hybrid robot achieves tool positioning including lumbar 4 (left), lumbar 4 (right), lumbar 3 (left), and lumbar 3 (right), based on the results of target path computation as shown in figure 14(c). Finally, to evaluate the experimental results, we obtain ap validation image and lateral validation image as shown in figure 14(d) and (e). According to the experimental results evaluated by surgeons, all the k-wires are in the acceptable area.

2) CADAVER EXPERIMENT

In order to further verify the ability of robotic system, we take cadaver as the subject. The experimental process is similar to spine model bone and the experimental results are shown in figure 15. Figure 15(a) and (b) are the validation fluoroscopy images with k-wires and pedicle screws. Figure 15(c) is the 3-D image derived from cadaver CT data.

In most of clinical studies, the accuracy is assessed by Gertzbein-Robbins classification [14], [17]. If the screw is fully within the pedicle, it is grade I. if screw deviation is <2 mm, it is considered as grade II. If the screw deviation is between 2mm and 4 mm, it is grade III. if screw deviation is >4 mm, it is considered as grade IV. In general, grades I and II are considered as acceptable [15]. In this experiment, 8 k-wires and the corresponding screws are placed in the lumbar spine level. According to both fluoroscopy images and 3-D image evaluated by surgeons, 6 of k-wires are fully within the pedicle and 2 k-wires in lumbar 2 are breach <2mm. Therefore, positions of all k-wires are acceptable.

In fact, k-wires placement in lumbar 2 have greater difficulty than the other lumbar levels. There are two main reasons. One is that the robotic system is instable due to the uncertain path planning and pool image quality. The other is that anatomical size of lumbar 2 is smaller than the other lumbar levels.

IV. CONCLUSION

In this paper, we propose a robot-assisted spine surgery system which not only meets the precision of lumbar level but also has low requirements for intraoperative imaging

equipment, based on intraoperative 2D fluoroscopy navigation and the corresponding procedure for robot-assisted spine surgery is designed. Next, hybrid robot is improved in structure parameters and joint drive compared with the first generation. Then, human-robot cooperation involving tool weight compensation and fuzzy variable admittance control are presented and could help assist in image acquisition and preliminary positioning of tool. In addition, the techniques within 2D navigation are described and noticed that a novel bi-planar design, a robust circular control point detector and closed-loop positioning of tool are introduced in navigation. Finally, the experiments related to kinematic model of hybrid robot in which the mean of distance error is selected as the accuracy performance, and tool weight compensation in which the max mean force error is selected as the accuracy performance, are implemented.

In experiments, the mean of distance error is 0.17 mm and could be acceptable because of much smaller than the motion range of hybrid robot (150 mm), the max mean force error is 0.7477 N and could be neglected compared with 30 N for tool weight and 10N for force exerted by operator. The torque error has similar results. Therefore, both kinematic model of hybrid robot and tool weight compensation could afford tasks in robotic system. In addition, we test the the robotic system proposed in this paper on spine model bone and cadaver with the help of surgeons. The k-wires position are validated by 2D image c-arm-based and 3D image CT-based and could be acceptable.

In cadaver experiment, 8 k-wires and screws are placed in the lumbar spine level. 6 of k-wires are grade I and 2 k-wires in lumbar 2 are grade II. In fact, k-wires placement in lumbar 2 have greater difficulty than the other lumbar levels because of uncertain path planning, pool image quality and smaller anatomical size of lumbar 2. The problems in robotic system would be further improved in the following research.

APPENDIXES

APPENDIX A

$$\boldsymbol{J}=\begin{bmatrix} 0 & 0 & 1 & 0 & f_1 \\ J_{21} & J_{22} & 0 & -f_1 f_{16} & f_2 f_5 \\ J_{31} & J_{32} & 0 & -f_1 f_5 & -f_2 f_{16} \\ -\frac{f_3}{f_{12}} & -\frac{f_4}{f_{12}} & 0 & 1 & 0 \\ -\frac{\tan\theta_5 f_3 f_5}{f_6} & -\frac{\tan\theta_5 f_4 f_5}{f_6} & 0 & \frac{\tan\theta_5 f_5}{f_{13} f_{16}^2} & -\frac{1+\tan\theta_5^2}{f_{13} f_{16}} \end{bmatrix} \tag{A.1}$$

where

$$\begin{aligned}
J_{21} &= \frac{f_{20}}{2l_{11}^2}+\frac{f_7}{2l_{11}}-\frac{L_1\sin(\gamma-f_{18})f_3}{f_{12}}+\frac{f_1 f_3 f_{16}}{f_{12}} \\
J_{22} &= \frac{f_9}{2l_{11}}-\frac{L_1\sin(\gamma-f_{18})f_4}{f_{12}}+\frac{f_1 f_4 f_{16}}{f_{12}} \\
J_{31} &= \frac{f_{14}}{f_{21}}+f_8+\frac{L_1\cos(\gamma-f_{18})f_3}{f_{12}}+\frac{f_1 f_3 f_5}{f_{12}} \\
J_{32} &= f_{10}-\frac{f_{15}}{f_{21}}+\frac{L_1\cos(\gamma-f_{18})f_4}{f_{12}}+\frac{f_1 f_4 f_5}{f_{12}} \\
f_1 &= L_2\cos\theta_5-d\sin\theta_5 \\
f_2 &= L_2\sin\theta_5-d\cos\theta_5 \\
f_3 &= \frac{f_{20}}{2l_{11}^2\sqrt{f_{19}}}+\frac{f_7}{2l_{11}\sqrt{f_{19}}} \\
&\quad -\frac{(\frac{f_{20}^2}{2l_{11}^3}+2(\frac{f_{14}}{f_{21}}+f_8)(l_{14}-\frac{f_{22}}{f_{21}})+\frac{f_7 f_{20}}{2l_{11}^2})f_{20}}{f_{11}} \\
f_4 &= \frac{f_9}{2l_{11}\sqrt{f_{19}}}+\frac{(2(l_{14}-\frac{f_{22}}{f_{21}})(f_{10}+1-\frac{f_{15}}{f_{21}})-\frac{f_9 f_{20}}{2l_{11}^2})f_{20}}{f_{11}} \\
f_5 &= \sin(\gamma+\theta+\theta_4-f_{18}) \\
f_6 &= f_{12} f_{13} f_{16}^2 \\
f_7 &= \frac{l_{14} f_{14}}{f_{23}}-2l_{11}+\frac{2l_{11} l_{14} f_{22}}{f_{23}^2} \\
f_8 &= \frac{4l_{11} f_{22}}{f_{21}^2} \\
f_9 &= 2l_{14}-\frac{f_{22}}{f_{23}}+\frac{2l_{14} f_{22}}{f_{23}^2}-\frac{l_{14} f_{15}}{f_{23}} \\
f_{10} &= \frac{4l_{14} f_{22}}{f_{21}^2} \\
f_{11} &= 4l_{11}\sqrt{f_{19}^3} \\
f_{12} &= \sqrt{1-\frac{f_{20}^2}{4l_{11}^2 f_{19}}} \\
f_{13} &= 1+\frac{\tan(\theta_5^2)}{f_{16}^2} \\
f_{14} &= \sqrt{f_{24} f_{25}}-2l_{11} l_{14}+\frac{l_{11}(2l_{11} f_{24}-2l_{11} f_{25})}{f_{17}} \\
f_{15} &= l_{11}^2+l_{12}^2-l_{13}^2+3l_{14}^2-\frac{l_{11}(2l_{14} f_{24}-2l_{14} f_{25})}{f_{17}} \\
f_{16} &= cos(\gamma+\theta+\theta_4-f_{18}) \\
f_{17} &= 2\sqrt{f_{24} f_{25}} \\
f_{18} &= \arccos(\frac{f_{20}}{2l_{11}\sqrt{f_{19}}}) \\
f_{19} &= (l_{14}-\frac{f_{22}}{f_{21}})^2+\frac{f_{20}^2}{4l_{11}^2} \\
f_{20} &= l_{11}^2-l_{12}^2+l_{13}^2-l_{14}^2+\frac{l_{14} f_{22}}{f_{23}} \\
f_{21} &= 2l_{11}^2+2l_{14}^2 \\
f_{22} &= l_{11}^2 l_{14}-l_{11}\sqrt{f_{24} f_{25}}+l_{11}^2 l_{14}-l_{13}^2 l_{14}+l_{14}^3 \\
f_{23} &= l_{11}^2+l_{14}^2 \\
f_{24} &= -l_{11}^2+l_{12}^2+2l_{12} l_{13}+l_{13}^2-l_{14}^2 \\
f_{25} &= l_{11}^2-l_{12}^2+2l_{12} l_{13}-l_{13}^2+l_{14}^2
\end{aligned}$$

APPENDIX B

See (B.1) at the next page.

$$\boldsymbol{J}^{-1} = \begin{bmatrix} 0 & N_{12} & N_{13} & N_{14} & N_{15} \\ 0 & N_{22} & -1 & N_{24} & N_{25} \\ 1 & 0 & 0 & 0 & g_{11} \\ 0 & \dfrac{2g_2}{g_8} & 0 & \dfrac{2g_7}{g_8}+1 & \dfrac{2g_9}{g_8} \\ 0 & 0 & 0 & 0 & -1 \end{bmatrix} \tag{B.1}$$

where

$$\begin{aligned}
N_{12} &= -\frac{2l_{13}\sin(g_{10})g_2}{g_8} - \frac{2L_1\cos(\gamma+g_{10})g_2g_6}{g_8g_3} \\
N_{13} &= -\frac{2z-2L_1\sin(\gamma+\mathrm{g}_{10})+2\cos(\theta_\mathrm{x})\mathrm{g}_{11}}{2g_3} \\
N_{14} &= \frac{(\sin\theta_x g_{11}-g_4)g_6}{g_3} - \frac{2l_{13}\sin(g_{10})g_7}{g_8} \\
N_{15} &= \frac{(g_1-g_5)g_6}{g_3} - \frac{2l_{13}\sin(g_{10})g_9}{g_8} \\
N_{22} &= -\frac{2L_1\cos(\gamma+g_{10})g_2}{g_8} - \frac{2l_{13}\cos(g_{10})g_2}{g_8} \\
N_{24} &= \sin(\theta_x)g_{11} - g_4 - \frac{2l_{13}\cos(g_{10})g_7}{g_8} \\
N_{25} &= g_1 - \frac{2l_{13}\cos(g_{10})g_9}{g_8} - g_5 \\
g_1 &= \cos(\theta_x)(L_2\sin(\theta_y) - d\cos(\theta_y)) \\
g_2 &= \frac{g_{12}}{g_{13}^2} - \frac{2L_2\cos(\theta_y)\sin(\theta_x) - 2y + 2d\sin(\theta_x)\sin(\theta_y)}{2g_{13}g_{14}} \\
g_3 &= \sqrt{l_{12}^2 - g_6^2} \\
g_4 &= \frac{2L_1\cos(\gamma+g_{10})g_7}{g_8} \\
g_5 &= \frac{2L_1\cos(\gamma+g_{10})g_9}{g_8} \\
g_6 &= z - L_1\sin(\gamma+g_{10}) + \cos(\theta_x)g_{11} \\
g_7 &= \frac{h_1+h_2-2y\cos(\theta_x)d\sin(\theta_y)}{2g_{13}g_{14}} - \frac{(L_2\cos(\theta_x)\cos(\theta_y)+d\cos(\theta_x)\sin(\theta_y))g_{12}}{g_{13}^2} \\
h_1 &= (2\cos(\theta_x)\sin(\theta_x)L_2^2\cos^2(\theta_y) + 4\cos(\theta_x)\sin(\theta_x)L_2d\cos(\theta_y)\sin(\theta_y) \\
h_2 &= -2y\cos(\theta_x)L_2\cos(\theta_y) + 2\cos(\theta_x)\sin(\theta_x)d^2\sin^2(\theta_y) \\
g_8 &= \frac{g_{12}^2}{g_{13}^2} + 1 \\
g_9 &= \frac{g_{12}(L_2\sin(\theta_x)\sin(\theta_y) - d\cos(\theta_y)\sin(\theta_x))}{g_{13}^2} - \frac{h_3+h_4}{2g_{13}g_{14}} \\
h_3 &= 2L_2^2\cos(\theta_y)\sin^2(\theta_x)\sin(\theta_y) - 2L_2d\cos^2(\theta_y)\sin^2(\theta_x) + 2L_2d\sin^2(\theta_x)\sin^2(\theta_y) \\
h_4 &= -2yL_2\sin(\theta_x)\sin(\theta_y) - 2d^2\cos(\theta_y)\sin^2(\theta_x)\sin(\theta_y) + 2yd\cos(\theta_y)\sin(\theta_x) \\
g_{10} &= 2\arctan(\frac{g_{12}}{g_{13}}) \\
g_{11} &= L_2\cos(\theta_y) + d\sin(\theta_y) \\
g_{12} &= g_{14} - L_1\sin\gamma \\
g_{13} &= l_{13} + y + L_1\cos\gamma - L_2\cos(\theta_y)\sin(\theta_x) - d\sin(\theta_x)\sin(\theta_y) \\
g_{14} &= \sqrt{h_5 - L_2^2\cos^2(\theta_y)\sin^2(\theta_x) - 2L_2d\cos(\theta_y)\sin^2(\theta_x)\sin(\theta_y) + h_6} \\
h_5 &= L_1^2\cos^2\gamma + L_1^2\sin^2\gamma + 2L_1l_{13}\cos\gamma \\
h_6 &= 2L_2y\cos(\theta_y)\sin(\theta_x) - d^2\sin^2(\theta_x)\sin^2(\theta_y) + 2dy\sin(\theta_x)\sin(\theta_y) + l_{13}^2 - y^2
\end{aligned}$$

REFERENCES

[1] K. Müeller, D. Zhao, O. Johnson, F. A. Sandhu, and J.-M. Voyadzis, "The difference in surgical site infection rates between open and minimally invasive spine surgery for degenerative lumbar pathology: A retrospective single center experience of 1442 cases," *Operative Neurosurg.*, vol. 16, no. 6, pp. 750–755, Jun. 2019.

[2] P. C. Hsieh, T. R. Koski, D. M. Sciubba, D. J. Moller, B. A. O'Shaughnessy, K. W. Li, Z. L. Gokaslan, S. L. Ondra, R. G. Fessler, and J. C. Liu, "Maximizing the potential of minimally invasive spine surgery in complex spinal disorders," *Neurosurg. Focus*, vol. 25, no. 2, p. E19, Aug. 2008.

[3] J. D. Castillo-Calcaneo, R. Navarro-Ramirez, M. Gimenez-Gigon, J. Adjei, A. Damolla, and J. Nakhla, "Principles and fundamentals of minimally invasive spine surgery," *World Neurosurg.*, vol. 119, pp. 465–471, Nov. 2018.

[4] C. D. Pannu, K. Farooque, V. Sharma, and D. Singal, "Minimally invasive spine surgeries for treatment of thoracolumbar fractures of spine: A systematic review," *J. Clin. Orthopaedics Trauma*, vol. 10, pp. S147–S155, Oct. 2019.

[5] S. Sharif and A. Afsar, "Learning curve and minimally invasive spine surgery," *World Neurosurg.*, vol. 119, pp. 472–478, Nov. 2018.

[6] G. Gebauer and D. G. Anderson, "Complications of minimally invasive lumbar spine surgery," *Seminars Spine Surgery*, vol. 23, no. 2, pp. 114–122, Jun. 2011.

[7] L. G. Lenke, "Point of view: Improved accuracy of pedicle screw insertion with computer-assisted surgery," *Spine*, vol. 22, no. 11, p. 1258, Jun. 1997.

[8] P. Merloz1, J. Troccaz, H. Vouaillat, C. Vasile, J. Tonetti, A. Eid, and S. Plaweski, "Fluoroscopy-based navigation system in spine surgery," *Proc. Inst. Mech. Eng. H, J. Eng. Med.*, vol. 221, no. 7, pp. 813–820, 2007.

[9] R. Navarro-Ramirez, G. Lang, X. Lian, C. Berlin, I. Janssen, A. Jada, M. Alimi, and R. Härtl, "Total navigation in spine surgery; A concise guide to eliminate fluoroscopy using a portable intraoperative computed tomography 3-Dimensional navigation system," *World Neurosurg.*, vol. 100, pp. 325–335, Apr. 2017.

[10] N.-F. Tian and H.-Z. Xu, "Image-guided pedicle screw insertion accuracy: A meta-analysis," *Int. Orthopaedics*, vol. 33, no. 4, pp. 895–903, Aug. 2009.

[11] A. Mason, R. Paulsen, J. M. Babuska, S. Rajpal, S. Burneikiene, E. L. Nelson, and A. T. Villavicencio, "The accuracy of pedicle screw placement using intraoperative image guidance systems," *J. Neurosurg., Spine*, vol. 20, no. 2, pp. 196–203, Feb. 2014.

[12] T. Jentzsch, K. Sprengel, L. Peterer, L. Mica, and C. M. L. Werner, "3D navigation of endoscopic rhizotomy at the lumbar spine," *J. Clin. Neurosci.*, vol. 23, pp. 101–105, Jan. 2016.

[13] J. M. Flynn and D. S. Sakai, "Improving safety in spinal deformity surgery: Advances in navigation and neurologic monitoring," *Eur. Spine J.*, vol. 22, no. S2, pp. 131–137, Mar. 2013.

[14] S. Divi, S. Pollster, E. Ramos, and M. J. Lee, "The current role of robotic technology in spine surgery," *Operative Techn. Orthopaedics*, vol. 27, no. 4, pp. 275–282, Dec. 2017.

[15] V. Solomiichuk, J. Fleischhammer, G. Molliqaj, J. Warda, A. Alaid, K. von Eckardstein, K. Schaller, E. Tessitore, V. Rohde, and B. Schatlo, "Robotic versus fluoroscopy-guided pedicle screw insertion for metastatic spinal disease: A matched-cohort comparison," *Neurosurg. Focus*, vol. 42, no. 5, p. E13, May 2017.

[16] J. L. Laratta, J. N. Shillingford, J. M. Lombardi, R. G. Alrabaa, B. Benkli, C. Fischer, L. G. Lenke, and R. A. Lehman, "Accuracy of S2 alar-iliac screw placement under robotic guidance," *Spine Deformity*, vol. 6, no. 2, pp. 130–136, Mar. 2018.

[17] A. Khan, J. E. Meyers, I. Siasios, and J. Pollina, "Next-generation robotic spine surgery: First report on feasibility, safety, and learning curve," *Operative Neurosurg.*, vol. 17, no. 1, pp. 61–69, Jul. 2019.

[18] A. Khan, J. E. Meyers, S. Yavorek, T. E. O'Connor, I. Siasios, J. P. Mullin, and J. Pollina, "Comparing next-generation robotic technology with 3-Dimensional computed tomography navigation technology for the insertion of posterior pedicle screws," *World Neurosurg.*, vol. 123, pp. e474–e481, Mar. 2019.

[19] N. Lonjon, E. Chan-Seng, V. Costalat, B. Bonnafoux, M. Vassal, and J. Boetto, "Robot-assisted spine surgery: Feasibility study through a prospective case-matched analysis," *Eur. Spine J.*, vol. 25, no. 3, pp. 947–955, Mar. 2016.

[20] M. Lefranc and J. Peltier, "Evaluation of the ROSA–spine robot for minimally invasive surgical procedures," *Expert Rev. Med. Devices*, vol. 13, no. 10, pp. 899–906, Oct. 2016.

[21] L. Chenin, J. Peltier, and M. Lefranc, "Minimally invasive transforaminal lumbar interbody fusion with the ROSATM spine robot and intraoperative flat-panel CT guidance," *Acta Neurochirurgica*, vol. 158, no. 6, pp. 1125–1128, Jun. 2016.

[22] Q. Zhang, X.-G. Han, Y.-F. Xu, Y.-J. Liu, B. Liu, D. He, Y.-Q. Sun, and W. Tian, "Robot-assisted versus fluoroscopy-guided pedicle screw placement in transforaminal lumbar interbody fusion for lumbar degenerative disease," *World Neurosurg.*, vol. 125, pp. e429–e434, May 2019.

[23] W. Tian, Y. Liu, B. Liu, D. He, J. Wu, X. Han, J. Zhao, M. Fan, "Guideline for thoracolumbar pedicle screw placement assisted by orthopaedic surgical robot," *Orthopaedic Surgery*, vol. 11, no. 2, pp. 153–159, Apr. 2019.

[24] S. Feng, W. Tian, Y. Sun, Y. Liu, and Y. Wei, "Effect of robot-assisted surgery on lumbar pedicle screw internal fixation in patients with osteoporosis," *World Neurosurg.*, vol. 125, pp. e1057–e1062, May 2019.

[25] G. B. Chung, S. Kim, S. G. Lee, B. J. Yi, W. Kim, S. M. Oh, Y. S. Kim, B. R. So, J. I. Park, and S. H. Oh, "An image-guided robotic surgery system for spinal fusion," *Int. J. Control, Automat., Syst.*, vol. 4, no. 1, pp. 30–41, 2006.

[26] J. Chung, S. Kim, B.-J. Yi, and Y. S. Kim, "Cadaver study for spinal fusion surgery using an image-guided surgical robot system," *Int. J. Control, Autom. Syst.*, vol. 8, no. 3, pp. 564–573, Jun. 2010.

[27] J. Lee, I. Hwang, K. Kim, S. Choi, W. K. Chung, and Y. S. Kim, "Cooperative robotic assistant with drill-by-wire end-effector for spinal fusion surgery," *Ind. Robot, Int. J.*, vol. 36, no. 1, pp. 60–72, Jan. 2009.

[28] T. Ortmaier, H. Weiss, U. Hagn, M. Grebenstein, M. Nickl, A. Albu-Schaffer, C. Ott, S. Jorg, R. Konietschke, L. Le-Tien, and G. Hirzinger, "A hands-on-robot for accurate placement of pedicle screws," in *Proc. IEEE Int. Conf. Robot. Autom. (ICRA)*, May 2006, pp. 4179–4186.

[29] S. Rezazadeh, W. Bai, M. Sun, S. Chen, Y. Lin, and Q. Cao, "Robotic spinal surgery system with force feedback for teleoperated drilling," *J. Eng.*, vol. 2019, no. 14, pp. 500–505, Feb. 2019.

[30] A. Bekku, J. Kim, Y. Nakajima, and K. Yonenobu, "A body-mounted surgical assistance robot for minimally invasive spinal puncture surgery," in *Proc. 5th IEEE RAS/EMBS Int. Conf. Biomed. Robot. Biomechtron.*, Aug. 2014, pp. 19–23.

[31] Y. Peng, H. Yu, and Z. Du, "Design and kinematic analysis of a hybrid manipulator for spine surgery," in *Proc. IEEE Int. Conf. Mechatronics Autom.*, Aug. 2016, pp. 884–889.

[32] N. Hogan, "Impedance control: An approach to manipulation," in *Proc. Amer. Control Conf.*, Jul. 1984, pp. 304–313.

[33] A. Lecours, B. Mayer-St-Onge, and C. Gosselin, "Variable admittance control of a four-degree-of-freedom intelligent assist device," in *Proc. IEEE Int. Conf. Robot. Autom.*, May 2012, pp. 3903–3908.

[34] B. Corteville, E. Aertbelien, H. Bruyninckx, J. De Schutter, and H. Van Brussel, "Human-inspired robot assistant for fast point-to-point movements," in *Proc. IEEE Int. Conf. Robot. Autom.*, Apr. 2007, pp. 3639–3644.

[35] D. Mao, W. Yang, and Z. Du, "Fuzzy variable impedance control based on stiffness identification for human-robot cooperation," *IOP Conf., Earth Environ. Sci.*, vol. 69, Jun. 2017, Art. no. 012090.

[36] A. Bertelsen, A. Garin-Muga, M. Echeverría, E. Gómez, and D. Borro, "Distortion correction and calibration of intra-operative spine X-ray images using a constrained DLT algorithm," *Comput. Med. Imag. Graph.*, vol. 38, no. 7, pp. 558–568, Oct. 2014.

[37] L. F. Gutierrez, G. Shechter, R. G. Lederman, E. R. McVeigh, and C. Ozturk, "Distortion correction, calibration, and registration: Towards an integrated MR and X-ray interventional suite," *Proc. SPIE*, vol. 5744, pp. 146–156, Apr. 2005.

[38] K. D. Gremban, C. E. Thorpe, and T. Kanade, "Geometric camera calibration using system of linear equations," in *Proc. ICRA*, 1988, pp. 562–567.

[39] S. Li, Z. Du, H. Yu, and J. Yi, "A robust multi-circle detector based on horizontal and vertical search analysis fitting with tangent direction," *Int. J. Pattern Recognit. Artif. Intell.*, vol. 33, no. 4, Apr. 2019, Art. no. 1954013.

[40] S. Li, Z. Du, H. Yu, J. Zhao, and X. Han, "A robust circular control point detector for bi-planar spine surgery navigation system," *IEEE Access*, vol. 6, pp. 71084–71098, 2018.

[41] H. A. Martins, J. R. Birk, and R. B. Kelley, "Camera models based on data from two calibration planes," *Comput. Graph. Image Process.*, vol. 17, no. 2, pp. 173–180, Oct. 1981.

[42] S. Lv, C. Meng, F. Zhou, B. Liu, and X. Zhou, "Visual model based C-arm system calibration and image correction," in *Proc. 2nd Int. Conf. Biomed. Eng. Informat.*, Oct. 2009, pp. 1–5.

[43] C. Meng, J. Zhang, F. Zhou, and T. Wang, "New method for geometric calibration and distortion correction of conventional C-arm," *Comput. Biol. Med.*, vol. 52, pp. 49–56, Sep. 2014.
[44] G. Zheng and X. Zhang, "Robust automatic detection and removal of fiducial projections in fluoroscopy images: An integrated solution," *Med. Eng. Phys.*, vol. 31, no. 5, pp. 571–580, Jun. 2009.
[45] H. Livyatan, Z. Yaniv, and L. Joskowicz, "Robust automatic C-arm calibration for fluoroscopy-based navigation: A practical approach," in *Proc. Med. Image Comput. Comput.-Assist. Intervent*, Sep. 2002, pp. 60–68.
[46] Y. Shiju, S. Yingying, W. Chengtao, and G. Lixu, "Proposal for conceptual designing of an innovative C-arm calibration target," in *Proc. 27th Annu. Conf. Eng. Med. Biol.*, 2005, pp. 6321–6324.
[47] S. Schumann, X. Dong, M. Puls, L. P. Nolte, and G. Zheng, "Calibration of C-arm for orthopedic interventions via statistical model-based distortion correction and robust phantom detection," in *Proc. Int. Symp. Biomed. Imag., Nano Macro*, 2012, pp. 1204–1207.
[48] S. Schumann, B. Thelen, S. Ballestra, L.-P. Nolte, P. Büchler, and G. Zheng, "X-ray image calibration and its application to clinical orthopedics," *Med. Eng. Phys.*, vol. 36, no. 7, pp. 968–974, Jul. 2014.
[49] T.-S. Fu, L.-H. Chen, C.-B. Wong, P.-L. Lai, T.-T. Tsai, C.-C. Niu, and W.-J. Chen, "Computer-assisted fluoroscopic navigation of pedicle screw insertion," *Acta Orthopaedica*, vol. 75, no. 6, pp. 730–735, Dec. 2004.
[50] B. Ravi, H. Bsc, A. Zahrai, and R. Rampersaud, "Clinical accuracy of computer-assisted two-dimensional fluoroscopy for the percutaneous placement of lumbosacral pedicle screws," *Spine*, vol. 36, no. 1, pp. 84–91, 2011.
[51] J. E. Webb, G. J. Regev, S. R. Garfin, and C. W. Kim, "Navigation-assisted fluoroscopy in minimally invasive direct lateral interbody fusion: A cadaveric study," *Int. J. Spine Surgery*, vol. 4, no. 4, pp. 115–121, Dec. 2010.
[52] M. Arand, S. Teller, F. Gebhard, M. Schultheiss, and P. Keppler, "Clinical accuracy of fluoroscopic navigation at the thoracic and lumbar spine," *Zeitschrift Orthopadie Unfallchirurgie*, vol. 133, no. 6, pp. 458–462, 2008.
[53] S. C. Thakkar, R. S. Thakkar, N. Sirisreetreerux, J. A. Carrino, B. Shafiq, and E. A. Hasenboehler, "2D versus 3D fluoroscopy-based navigation in posterior pelvic fixation: Review of the literature on current technology," *Int. J. Comput. Assist. Radiol. Surgery*, vol. 12, no. 1, pp. 69–76, Jan. 2017.
[54] B. G. Ochs, C. Gonser, T. Shiozawa, A. Badke, K. Weise, B. Rolauffs, and F. M. Stuby, "Computer-assisted periacetabular screw placement: Comparison of different fluoroscopy-based navigation procedures with conventional technique," *Injury*, vol. 41, no. 12, pp. 1297–1305, Dec. 2010.
[55] L. Hu, S. Luan, M. Wang, J. Wang, and W. Liu, "A biplanar robot navigation system for the distal locking of intramedullary nails," *Int. J. Med. Robot. Comput.*, vol. 1, no. 1, pp. 61–65, 2010.
[56] V. Duchaine and C. M. Gosselin, "General model of human-robot cooperation using a novel velocity based variable impedance control," in *Proc. 2nd Joint EuroHaptics Conf. Symp. Haptic Inter. Virtual Environ. Teleoperator Syst. (WHC)*, Mar. 2007, pp. 22–24.
[57] F. Dimeas and N. Aspragathos, "Online stability in human-robot cooperation with admittance control," *IEEE Trans. Haptics*, vol. 9, no. 2, pp. 267–278, Apr. 2016.

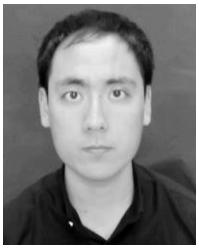

SHAODONG LI received the master's degree in mechanical and electronic engineering from Northeastern University, China, in 2015. He is currently pursuing the Ph.D. degree with the State Key Laboratory of Robotics and System, Harbin Institute of Technology. His research interests are in the areas of robot-assisted surgery navigation system, including image processing, registration, and pattern recognition.

ZHIJIANG DU received the Ph.D. degree in mechanical and electronic engineering from the Harbin Institute of Technology, China, in 2001. He is currently a Professor with the Harbin Institute of Technology. His research interests are in the areas of medical robot, industrial robot, and navigation.

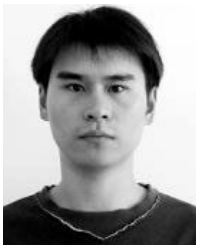

HONGJIAN YU received the Ph.D. degree in mechanical and electronic engineering from the Harbin Institute of Technology, China, in 2010. He is currently with the Harbin Institute of Technology. His research interests are in the areas of parallel manipulator system and pattern recognition.